Letter Vol. 43, No. 24 / 15 December 2018 / Optics Letters 6009

Optics Letters

Measurement of high pressure and high temperature using a dual-cavity Fabry–Perot interferometer created in cascade hollow-core fibers

Zhe Zhang, Jun He,* Bin Du, Fengchan Zhang, Kuikui Guo, and Yiping Wang

Key Laboratory of Optoelectronic Devices and Systems of Ministry of Education and Guangdong Province, College of Optoelectronic Engineering, Shenzhen University, Shenzhen 518060, China

**Corresponding author: hejun07@szu.edu.cn*

Received 21 September 2018; revised 8 November 2018; accepted 8 November 2018; posted 9 November 2018 (Doc. ID 346526); published 11 December 2018

A compact dual-cavity Fabry–Perot interferometer (DC-FPI) sensor is proposed and demonstrated based on a hollow-core photonic bandgap fiber (HC-PBF) spliced with a hollow-core fiber (HCF). The HC-PBF, which has low transmission loss, was used as the first FPI cavity and also acted as a bridge between the lead-in single-mode fiber and the HCF. The HCF was used as the second FPI cavity and also acted as a micro gas inlet into the first FPI cavity. A DC-FPI sensor with different cavity lengths of 226 and 634 μm in the first FPI and the second FPI was created. Both gas pressures ranging from 0–10 MPa and temperatures ranging from 100–800°C were measured using the DC-FPI sensors together with a fast Fourier transform and phase-demodulation algorithm. Experimental results showed that the first FPI cavity was gas pressure sensitive but temperature insensitive, while the second FPI cavity was temperature sensitive but gas pressure insensitive. A high gas pressure sensitivity of 1.336 μm/MPa and a temperature sensitivity of 17 nm/°C were achieved in the DC-FPI sensor. Moreover, the cross sensitivity between the gas pressure and temperature was calculated to be ∼ − 15 Pa/°C and ∼0.3°C/MPa. The proposed DC-FPI sensors provide a promising candidate for the simultaneous measurement of high pressures and high temperatures at some precise locations.

https://doi.org/10.1364/OL.43.006009

The simultaneous measurement of high pressures and high temperatures is of significant importance in a variety of industrial applications. Over the past few decades, fiber Bragg gratings (FBGs) and fiber Fabry–Perot interferometers (FPIs) have been widely studied for use in the measurement of temperature and pressure, respectively [1]. Various fiber-tip FPIs have been demonstrated with extremely high pressure sensitivities [2,3]. Hybrid structures have also been reported recently, including FBG/FPI and FPI/FPI, for measuring temperature and pressure simultaneously [4–6]. For example, FBG/FPI hybrid structures have been produced by cascading an FBG and an FPI [4]. However, the operational temperature of these FBG/FPI hybrid sensors was limited by the FBG, which typically exhibits a poor thermal stability at temperatures higher than 300°C. Moreover, the FPI/FPI hybrid structure is a promising way for the simultaneous measurement of high pressures and high temperatures [5]. However, the previous reported FPI/FPI hybrid structures were fabricated using either chemical etching [5] or laser micromachining [6], each of which requires a complicated series of steps and expensive equipment. Hence, a simple and cost-effective sensor for high gas pressure and temperature measurements has yet to be developed.

As such, we employ a hollow-core photonic bandgap fiber (HC-PBF) to develop a new high-pressure and high-temperature sensor. The HC-PBF guides optical modes in its air core surrounded by a microstructured cladding, which is formed by periodic arrays of airholes running along the fiber. These guided optical modes were tightly confined to the air core. The HC-PBF has a low transmission loss, and its unique microstructure facilitates the simultaneous confinement of light and material in the air core, providing an excellent platform for strong light–matter interactions over long distances. HC-PBFs have been reported for use in the design of microfluidic biological reactors [7,8], composition analysis of trace gases [9,10], acoustic pressure sensing [11,12], fabrication of gas or dye lasers [13], optomechanical trapping of nanoparticles and nanospikes [14,15], high-power laser beam shaping [16], Raman spectroscopy [17], and transmission of megawatt optical signals [16]. More importantly, air exhibits much weaker thermo-optical effects than silica, which makes the HC-PBF an ideal candidate for fabricating temperature-insensitive photonic devices, including optical fiber gyroscopes [18], optoelectronic oscillators [19], and novel fiber-optic sensors.

In this Letter, a dual-cavity FPI (DC-FPI) sensor is proposed and demonstrated for the simultaneous measurement of gas pressure and temperature in a wide range of 0–10 MPa and 100–800°C, respectively. This DC-FPI was constructed by interposing a section of HC-PBF between a lead-in single-mode fiber (SMF) and a section of hollow-core fiber (HCF). The HC-PBF acted as both the first cavity (cavity 1) and an excellent photonic waveguide. The HCF, with an inner diameter of ~2 μm, acted as both the second cavity (cavity 2) and a microfluidic channel for gas inlet into cavity 1. Gas pressure and temperature were simultaneously measured using a fast Fourier transform (FFT) and phase demodulation algorithm. Moreover, the proposed DC-FPI sensor is simple to fabricate and exhibits a high sensitivity and stability in a wide measurement range. As far as we are concerned, this study also represents the first simultaneous measurement of a temperature higher than 800°C and a gas pressure exceeding 10 MPa.

The proposed DC-FPI structure is illustrated in Fig. 1(a), where a section of HC-PBF is spliced between a lead-in SMF and an HCF. Both the HC-PBF and the HCF are made by pure silica, which has a thermo-optic coefficient of $\alpha_0 = \sim 1.25 \times 10^{-5}/°C$ [20] and a thermal expansion coefficient of $\alpha_e = \sim 0.55 \times 10^{-6}/°C$ [21]. In addition, the core diameter in HC-PBF is ~10.9 μm, which is much larger than the core diameter in HCF (~2 μm). The smaller core diameter in HCF than HC-PBF results not only in a reflective surface at the interface between the HC-PBF and HCF (i.e., interface II), but also in the light coupling between the HC-PBF air core and the HCF silica cladding. Moreover, the free end of the HCF is cleaved, and a flat reflective surface (i.e., interface III) is created. As illustrated in Fig. 1(a), the reflections from the three interfaces (i.e., interface I, II, and III) are collected and transmitted back to the lead-in SMF, resulting in a three-beam interference spectrum. The HC-PBF acts as cavity 1, in which light transmits through the air core of HC-PBF with low transmission loss. The HCF acts as cavity 2, in which light transmits through the silica cladding of HCF. In this configuration, the HCF also functions as a microfluidic channel for the gas inlet. As the gas pressure changes, the refractive index (RI) of the air in the HC-PBF core varies as [22]

$$n = 1 + \frac{2.8793 \times 10^{-9}}{1 + 0.00367 \times T} P, \tag{1}$$

where n is the RI of the air, P is the gas pressure (Pa), and T is the environmental temperature (°C). The variation in RI caused by gas pressure changes alters the absolute optical path difference (OPD) in cavity 1 significantly. Nevertheless, the variation in RI induced by temperature changes is quite small and has little influence on the OPD in cavity 1. From Eq. (1), the cross sensitivity between gas pressure and temperature can be estimated to be 268 Pa/°C at the atmospheric pressure and the temperature of 100°C. As a result, cavity 1 can be utilized as a gas pressure sensor. In contrast, as cavity 2 was formed by a silica medium, the OPD in cavity 2 varies significantly with temperature due to the thermo-optic and thermo-expansion effects. However, it could hardly change with the gas pressure. As such, cavity 2 can be utilized as a temperature sensor. It is worth noting the HC-PBF plays a vital role in this configuration due to its low transmission loss. This ensures sufficient intensity of light reflected from the HCF end face, resulting in high visibility in the reflection spectrum for demodulation. Theoretically, the length of the HC-PBF and HCF can be increased to obtain a higher gas pressure and temperature sensitivity in the proposed DC-FPI sensors.

The fabrication process of a DC-FPI sensor includes four steps. At first, an HC-PBF (NKT, HC-1550-2) was spliced with an SMF using a commercial fusion splicer (Fujikura, FSM-60S) with optimized parameters. Subsequently, the HC-PBF was cleaved by a fiber cleaver under the surveillance of a CCD camera so that the length of the HC-PBF was precisely controlled. And then the cleaved HC-PBF was spliced with a pure silica HCF using the same method. Finally, the HCF was precisely cleaved to the desired length. It is worth noting the fusion splicing parameters for different fibers were optimized to produce minimal losses. The utilized HC-PBF had an air core diameter of ~10.9 μm, which was surrounded by an airhole cladding lattice with an average pitch value of ~3.8 μm. This honeycomb cladding had a diameter of ~70 μm and was surrounded by a ring of solid silica. The total diameter of the HC-PBF was ~120 μm. Moreover, the HCF was composed of a pure silica capillary with inner and outer diameters of ~2 and 125 μm, respectively. Figure 1(b) shows an optical microscope image of a fabricated DC-FPI sensor (S1). Four different DC-FPI sensors (S1–S4) of varying FPI cavity lengths were fabricated using this method. The DC-FPI sensors S1–S4 have an FPI cavity 1 length of 226, 261, 242, and 621 μm, and an FPI cavity 2 length of 634, 751, 957, and 1491 μm, respectively. The morphologies and corresponding reflection spectra of these DC-FPI sensors are illustrated in Fig. 2. It is clear that increasing the HC-PBF length

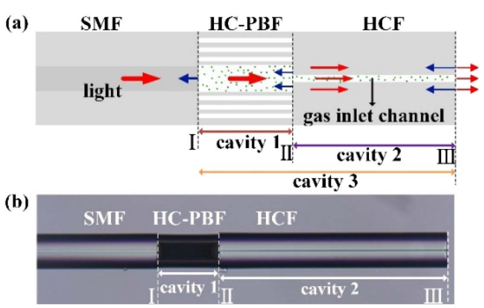

Fig. 1. (a) Schematic diagram of the proposed DC-FPI sensor. (b) Side-view microscopy images of the fabricated DC-FPI sensor. HCF, hollow-core fiber; HC-PBF, hollow-core photonic bandgap fiber; SMF, single-mode fiber.

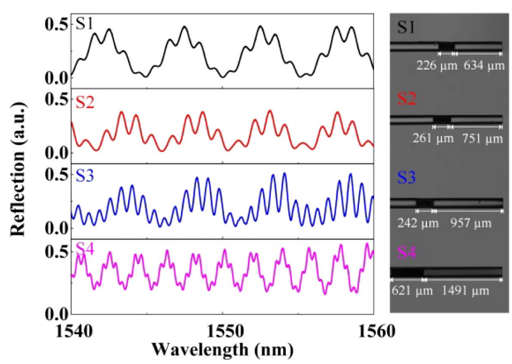

Fig. 2. Reflection spectra and corresponding microscopy images of the four fabricated DC-FPI sensors (S1–S4) with varying FPI cavity lengths. The reflection spectra were measured at atmospheric pressure and room temperature.

leads to a degeneration in the interference fringe visibility of the DC-FPI sensor. As a result, we chose the DC-FPI sensor S1 for the following gas pressure and temperature measurements.

The gas pressure tests were conducted using an experimental setup similar to that in our previous study [23]. The wavelength resolution of the optical spectrum analyzer (OSA) (Yokogawa, AQ6370C) was set to 0.02 nm. The reflection spectrum of the DC-FPI sensor at the room temperature and atmospheric pressure is shown in Fig. 3(a). As expected, a superimposed spectrum from FPI cavity 1 and FPI cavity 2 can be observed. Figure 3(b) shows the FFT results of the spectrum in Fig. 3(a), where three primary frequency components at ∼0.2, 0.8, and 1.0 Hz are evident. A higher-order reflection, caused by the low finesse of the FPIs, was suppressed. Two bandpass filters with ranges of 0.1–0.3 and 0.7–0.9 Hz were applied to the reflection spectra for cavity 1 and cavity 2, which were separated and are displayed in Figs. 3(c) and 3(d), respectively. The relative phase shift $\Delta\varphi$ generated by wavelength scanning from λ_1 to λ_2 could be accurately obtained by the Fourier phase demodulation method [24,25]. Hence, the absolute OPD can be determined by

$$\mathrm{OPD} = \frac{\lambda_1\lambda_2}{4\pi(\lambda_1 - \lambda_2)}\Delta\varphi. \tag{2}$$

The gas pressure was increased from 0–10 MPa with a step size of 1 MPa. At each determined gas pressure, the reflection spectrum for the DC-FPI sensor was recorded by an OSA, and the OPDs of the two cavities were demodulated as described previously. Figure 4 shows the gas pressure sensitivities of the two cavities. Cavity 1 exhibited a sensitivity of ∼1.336 μm/MPa, which is approximately 2 orders of magnitude higher than cavity 2 (∼0.008 μm/MPa). The gas pressure sensitivity of this DC-FPI sensor is similar to that reported in [26], whereas the measured gas pressure range and temperature range of the DC-FPI sensor are significantly larger than those results demonstrated in [26].

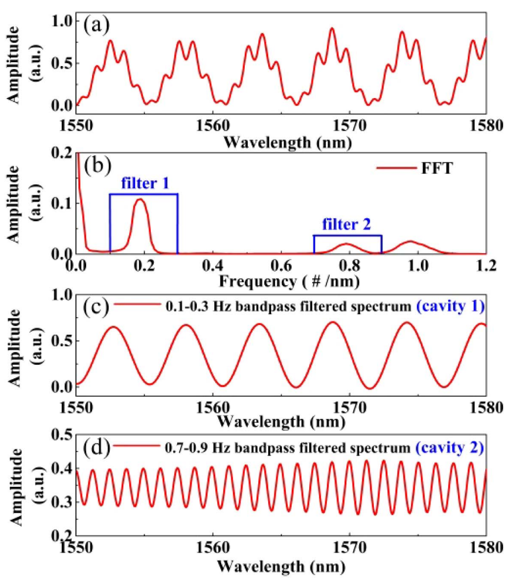

Fig. 3. (a) Reflection spectrum of the DC-FPI sensor and (b) its corresponding FFT spectrum and the application of two bandpass filters. Also shown are the recovered reflection spectra of (c) cavity 1 and (d) cavity 2 after bandpass filtering.

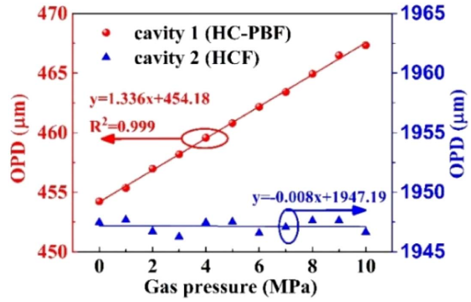

Fig. 4. Optical path difference (OPD) for the two cavities in the DC-FPI as a function of gas pressure.

The high-temperature performance of the DC-FPI sensor was tested using the same setup described in our previous study [27]. The temperature was first increased from 100 to 800°C with a step size of 100°C. Each temperature was maintained for ∼15 min to acquire a stable reflection spectrum. The temperature was then decreased from 800 to 100°C with the same step size. An annealing process was conducted by repeating these heating and cooling cycles three times over a period of three days. The relationship between OPD and applied temperature, obtained by demodulating each recorded spectrum, is plotted for the two cavities in Fig. 5. The temperature sensitivity of cavity 2, acquired using a linear fit, was ∼17 nm/°C, which is approximately 2 orders of magnitude higher than cavity 1 (∼0.1 nm/°C). After a series of gas pressure and temperature tests, the DC-FPI sensor was removed from the oven. The resulting morphology is shown in Fig. 6, where it is evident the DC-FPI sensor remained an intact structure.

The gas pressure measurement errors generated from cavity 1 (caused by temperature drifts) were calculated to be ∼74 Pa/°C, which is approximately 2 orders of magnitude smaller than the errors in our previous work [2]. The temperature measurement errors generated from cavity 2 (caused by

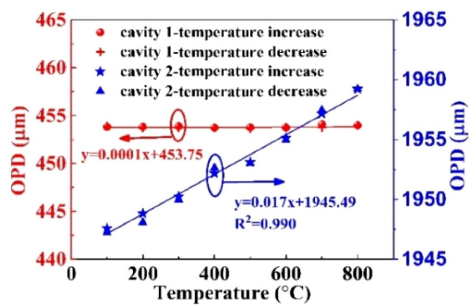

Fig. 5. Optical path difference (OPD) for the two cavities in the DC-FPI as a function of temperature.

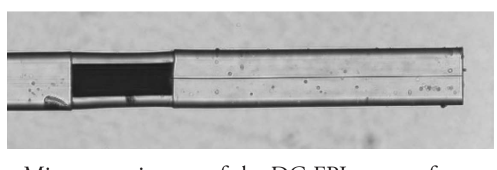

Fig. 6. Microscopy images of the DC-FPI sensor after conducting high-pressure and high-temperature tests.

gas pressure changes) were negligible (i.e., ~ – 0.47°C/MPa). It is worth noting that the linearity of the DC-FPI sensor is not ideal, which may be attributed to the errors in reading the peak or dip wavelength. As such, phase demodulation algorithms capable of achieving higher accuracy are in demand, and it will be the emphasis of our ongoing research.

The gas pressure sensitivity of cavity 1 can be expressed as

$$\frac{d(\mathrm{OPD})}{dP} = 2n_1\frac{dL_1}{dP} + 2L_1\frac{dn_1}{dP}, \tag{3}$$

where P represents gas pressure, n_1 is the RI of air, and L_1 is the length of cavity 1. In these tests, L_1 was measured to be ~226 μm, dn_1/dP can be calculated from Eq. (1) at room temperature $T \approx 25°\mathrm{C}$, and dL_1/dP depends on the Young's modulus of the HC-PBF. From Eq. (3), it is evident the gas pressure sensitivity of cavity 1 demonstrates a positive correlation with the cavity length L_1. By increasing the length of HC-PBF, a higher gas pressure sensitivity could be achieved without compromising the fringe visibility in cavity 2, resulting from the low transmission loss in the HC-PBF.

The temperature sensitivity of cavity 2 can be attributed to the thermo-optic and thermoexpansion effects in silica material. The temperature sensitivity of cavity 2 can be expressed as

$$\frac{d(\mathrm{OPD})}{dT} = 2n_2\frac{dL_2}{dT} + 2L_2\frac{dn_2}{dT}, \tag{4}$$

where T represents temperature, n_2 is the RI of silica, and L_2 is the length of cavity 2. In these experiments, L_2 was measured to be ~634 μm. As discussed previously, the thermo-optical coefficient of silica ($\alpha_0 = \sim 1.25 \times 10^{-5}/°\mathrm{C}$) is approximately 2 orders of magnitude larger than its thermoexpansion coefficient ($\alpha_e = \sim 0.55 \times 10^{-6}/°\mathrm{C}$). Hence, the second term in Eq. (4) will dominate the temperature sensitivity of cavity 2. Moreover, the temperature drift-induced OPD changes in cavity 1 will be much lower due to the much smaller thermo-optical coefficient [as shown in Eq. (1)] and much smaller thermoexpansion coefficient in the air core of HC-PBF. In addition, the temperature sensitivity can be improved by increasing L_2. However, the fringe visibility in the reflection spectrum of cavity 2 will decrease significantly due to the large transmission loss in the HCF. Consequently, the cavity length L_2 is a trade-off between the sensitivity and fringe visibility.

In summary, a compact DC-FPI sensor has been proposed and demonstrated based on an HC-PBF and an HCF. The HC-PBF acts as both cavity 1 and a low-loss optical waveguide, while the HCF acts as both cavity 2 and a microchannel for the gas inlet into cavity 1. The two FPI cavities were sensitive to changes in gas pressure and temperature, respectively, while insensitive to other conditions. Gas pressures over a range of 0–10 MPa and temperatures over a range of 100–800°C were determined simultaneously using a FFT and a phase demodulation algorithm. Experimental results showed DC-FPI sensors with cavity lengths of 226 and 634 μm exhibited a gas pressure sensitivity of 1.336 μm/MPa and a temperature sensitivity of 17 nm/°C. Moreover, the cross sensitivities between gas pressure and temperature were calculated to be ~74 Pa/°C and ~ – 0.47°C/MPa, which is several orders of magnitude lower than previous reports. These low cross sensitivities make the DC-FPI sensor attractive for simultaneous measuring of high gas pressures and high temperatures. In addition, the phase sensitivity of the DC-FPI sensor can be further increased by increasing the length of the two cavities. This compact sensor structure featured a diameter of ~125 μm and a total length of ~1 mm, making it an ideal candidate for simultaneous measuring of high pressures and high temperatures in some precise locations.

Funding. National Natural Science Foundation of China (NSFC) (61875128, 61635007); Natural Science Foundation of Guangdong Province (2017A010102015); Science and Technology Innovation Commission of Shenzhen (JCYJ20170302143105991, JCYJ20170412105604705); Research Funding from Shenzhen University (2017019); Development and Reform Commission of Shenzhen Municipality Foundation

REFERENCES

1. C. Liao, Y. H. Li, D. Wang, T. Sun, and K. Grattan, IEEE Sens. J. **10**, 1675 (2010).
2. Z. Zhang, C. Liao, J. Tang, Z. Bai, K. Guo, M. Hou, J. He, Y. Wang, S. Liu, F. Zhang, and Y. Wang, J. Lightwave Technol. **35**, 4067 (2017).
3. J. Ma, W. Jin, H. Ho, and J. Dai, Opt. Lett. **37**, 2493 (2012).
4. N. Dong, S. Wang, L. Jiang, Y. Jiang, P. Wang, and L. Zhang, IEEE Photon. Technol. Lett. **30**, 431 (2018).
5. S. Pevec and D. Donlagic, Appl. Opt. **51**, 4536 (2012).
6. Y. Zhang, J. Huang, X. Lan, L. Yuan, and H. Xiao, Opt. Eng. **53**, 067101 (2014).
7. P. J. Sazio, A. Amezcuacorrea, C. E. Finlayson, J. R. Hayes, T. J. Scheidemantel, N. F. Baril, B. R. Jackson, D. J. Won, F. Zhang, E. R. Margine, V. Gopalan, V. H. Crespi, and J. V. Badding, Science **311**, 1583 (2006).
8. S. Unterkofler, R. J. McQuitty, T. G. Euser, N. J. Farrer, P. J. Sadler, and P. St.J. Russell, Opt. Lett. **37**, 1952 (2012).
9. W. Jin, Y. Cao, F. Yang, and H. Ho, Nat. Commun. **6**, 6767 (2015).
10. F. Yang, Y. Tan, W. Jin, Y. Lin, Q. Yun, and H. Ho, Opt. Lett. **41**, 3025 (2016).
11. J. Lægsgaard and P. J. Roberts, J. Opt. Soc. Am. B **26**, 1795 (2009).
12. R. E. P. D. Oliveira, C. J. S. D. Matos, J. G. Hayashi, and C. M. B. Cordeiro, J. Lightwave Technol. **27**, 1605 (2009).
13. F. Couny, F. Benabid, and P. S. Light, Phys. Rev. Lett. **99**, 143903 (2007).
14. P. St.J. Russell, R. Pennetta, and S. Xie, Optica **3**, 277 (2016).
15. R. Zeltner, S. Xie, R. Pennetta, and P. St.J. Russell, ACS Photon. **4**, 378 (2017).
16. G. Humbert, J. C. Knight, G. Bouwmans, P. St.J. Russell, D. P. Williams, P. J. Roberts, and B. J. Mangan, Opt. Express **12**, 1477 (2004).
17. S. O. Konorov, C. J. Addison, H. G. Schulze, R. F. Turner, and M. W. Blades, Opt. Lett. **31**, 1911 (2006).
18. M. Digonnet, S. Blin, H. K. Kim, V. Dangui, and G. Kino, Meas. Sci. Technol. **18**, 3089 (2007).
19. U. S. Mutugala, J. Kim, T. D. Bradley, N. V. Wheeler, S. R. Sandoghchi, J. R. Hayes, E. Numkam Fokoua, F. Poletti, M. N. Petrovich, D. J. Richardson, and R. Slavík, Opt. Lett. **42**, 2647 (2017).
20. J. H. Wray and J. T. Neu, J. Opt. Soc. Am. B. **59**, 774 (1969).
21. B. Kuhn and R. Schadrack, J. Non-Cryst. Solids **355**, 323 (2009).
22. M. Deng, C. Tang, T. Zhu, Y. Rao, L. Xu, and M. Han, Appl. Opt. **49**, 1593 (2010).
23. Z. Zhang, J. He, Q. Dong, Z. Bai, C. Liao, Y. Wang, S. Liu, K. Guo, and Y. Wang, Opt. Lett. **43**, 3017 (2018).
24. Y. Jiang, IEEE Photon. Technol. Lett. **20**, 75 (2008).
25. Y. Jiang and C. Tang, Rev. Sci. Instrum. **79**, 106105 (2008).
26. H. Bae and M. Yu, Opt. Express **20**, 14573 (2012).
27. Z. Zhang, C. Liao, J. Tang, Y. Wang, Z. Bai, Z. Li, K. Guo, M. Deng, S. Cao, and Y. Wang, IEEE Photon. J. **9**, 7101109 (2017).